Oxygen partitioning into biomolecular condensates is governed by excluded volume

Ankush Garg[1,2], Christopher Brasnett[3], Siewert J. Marrink[3], Klaus Koren[4], Magnus Kjaergaard[1,2,5]*

1 Department of Molecular Biology and Genetics, Aarhus University, Denmark

2 Interdisciplinary Nanoscience Center (iNANO), Aarhus University, Denmark

3 Groningen Biomolecular Sciences and Biotechnology Institute, University of Groningen, Nijenborgh 7, 9747 AG Groningen, The Netherlands

4 Department of Biology, Aarhus University, Denmark

5 The Danish Research Center for Translational Neuroscience, Aarhus University, Denmark

*= corresponding author. (magnus@mbg.au.dk)

ORCID:

A.G.: 0000-0002-8369-5017

C.B.: 0000-0001-9235-1673

S.J.M.: 0000-0001-8423-5277

K.K.: 0000-0002-7537-3114

M.K.: 0000-0002-7020-9366

Abstract:

Biomolecular condensates form through the self-assembly of proteins and nucleic acids to create dynamic compartments in cells. By concentrating specific molecules, condensates establish distinct microenvironments that regulate biochemical reactions in time and space. Macromolecules and metabolites partition into condensates depending on their interactions with the macromolecular constituents, however, the partitioning of gases has not been explored. We investigated oxygen partitioning into condensates formed by intrinsically disordered repeat proteins with systematic sequence variations using phosphorescence lifetime imaging microscopy (PLIM). Unlike other hydrophobic metabolites, oxygen is partially excluded from the condensate with partitioning constants more strongly modulated by changes in protein length than hydrophobicity. For repeat proteins, the dense phase protein concentration drops with chain length resulting in a looser condensate with less excluded volume. We found that oxygen partitioning is anti-correlated with dense phase protein concentration, suggesting that oxygen concentration is mainly determined by the solvent accessible volume. This suggests that oxygen partitioning is determined by the physical organization of the condensates rather than the chemical properties of the scaffold. Molecular dynamics simulations suggest that oxygen does not form strong and specific interactions with the scaffold and is dynamic on the nanosecond timescale. Biomolecular condensates thus result in variation of oxygen concentrations on nanometer length-scales, which can tune the oxygen concentration available for biochemical reactions within the cell.

Introduction

Oxygen gradients form throughout biology when the rate of consumption exceeds the rate at which it can be replenished by diffusion. Oxygen gradients are well documented on meter scales in the ocean due to the respiration of organic matter, or on centimeter scales in e.g. lake bottoms (1–3). In our blood circulation, oxygen gradients occur on sub-millimeter scales across alveoli and arteries, where oxygenated blood releases oxygen to tissues (4). Diffusion works more efficiently at short length scales, and therefore it is increasingly difficult for oxygen gradients to arise. However, it has been speculated that oxygen gradients could also arise on a sub-cellular length scale, but this has been difficult to test experimentally. Nonetheless, oxygen gradients have been reported in giant umbrella cells, where deoxygenated regions formed around mitochondria due aerobic respiration (5). Similarly, swimming bacteria are capable of detecting changes in oxygen on µm scale of their long axis (6). Here we investigate an additional mechanism whereby oxygen gradients might arise on a subcellular length scale: passive partitioning into membrane-less organelles.

Cells are compartmentalized into several compartments. In addition to the traditional organelles, a new type of compartments have recently been identified that form by condensation of biomolecules, so-called biomolecular condensates, or membrane-less organelles (7,8). Like traditional organelles, membrane-less organelles can regulate biochemical reactions by spatial confinement – some components are concentrated, and others are excluded (9). Unlike traditional organelles, membrane-less ones can form and dissolve and thus serve as a trigger for changes in cellular metabolism or signaling (10,11). Oxygen is the ultimate oxidizing agent in most of our metabolism and thus takes part in many biochemical reactions, and in undesired side reactions for others. To understand how membrane-less organelles affect oxygen-dependent cellular processes, it is thus necessary to understand how oxygen partitions into biomolecular condensates.

Biomolecular condensates concentrate or exclude molecules through chemical partition equilibria. Condensates have different interior milieu compared to the bulk cytosol that form solvation-like interactions with other molecules and thus act as a distinct solvent phase (12,13). Macromolecules like proteins and RNA can be concentrated by thousands of folds or excluded because the

condensate forms a mesh with pores too small to accommodate molecules beyond a certain size. Comparatively little is known about the partitioning of small molecules into condensates as these cannot easily be tagged with a fluorophore. Using fluorescence microscopy to quantify partitioning, it has been shown that condensates up-concentrate a range of small molecules in vitro and in cells (14–16), and that the protein scaffold creates distinct chemical environments that concentrate specific molecules. These studies were, however, limited to the study of fluorophores and thus mostly aromatic compounds. Mass spectrometry approaches developed for metabolomics allow investigation of a broader range of metabolites and drug-like compounds (17,18). This led to the conclusion that small molecule partitioning did not depend on high affinity binding with scaffold protein or pore size, but rather depended on solvent properties of the condensates, principally hydrophobicity. Investigation of condensate metabolomes in cells further showed that especially phospholipids are enriched in condensates (17).

A key challenge for the study of the sub-cellular oxygen gradients has been a scarcity of methods to detect such gradients. Phosphorescence lifetime imaging microscopy (PLIM) is currently the oxygen imaging technique with the highest spatial resolution. Some transition metal dye molecules display oxygen sensitive phosphorescence lifetimes, which has been developed into a series of probe molecules used for PLIM. The presence of heavy metals in these phosphorescent probes allows the efficient intersystem crossing from singlet excited state to triplet excited state leading to phosphorescence (19,20). The phosphorescence of these metal complex dyes, called indicators, gets quenched by molecular oxygen by the process of energy transfer from the indicator to the oxygen. We speculated that these dyes could be used to measure oxygen gradients inside biomolecular condensates as well.

In the present work, we measured oxygen partitioning in the biomolecular condensates using PLIM, and found that oxygen concentrations are generally decreased inside condensates, a finding corroborated by molecular dynamics (MD) simulations. Our research highlights that oxygen partitioning is dominated by the accessible solvent volume rather than chemical properties of the scaffold.

Materials and methods:

Protein expression and purification:

Genes encoding octapeptide repeat protein [$Q_{5,8}$]-20, [$Q_{5,8}$]-30, [$Q_{5,8}$]-40, [$Q_{5,8}$]-60, [(3$Q_{5:}V_5$),Q_8]-60, [($Q_{5:}V_5$),Q_8]-60 and [V_5,Q_8]-60 were synthesized and then cloned between the NdeI and BamHI sites in a pET-15b vector by Genscript (Table S1). Plasmids were transformed into chemical competent *E. coli* BL21(DE3) and grown at 37 °C in terrific broth containing 100 µg/mL ampicillin and 180 rpm shaking till stationary phase, where protein expression was induced with 0.5 mM IPTG and incubated for next 14-16 hours. Cells were harvested by centrifugation at 4000 g for 30 mins.

Repeat proteins were purified as reported with minor modifications (21). Briefly, cell pellet was dissolved in milli-Q water and lysed by probe sonication and pelleted by centrifugation (13,000 g, 30 min). The pellet was dissolved in a buffer (pH 7.4) containing 8 M urea, 150 mM K_2HPO_4/KH_2PO_4, and 150 mM NaCl. Cell debris was cleared by centrifugation. The protein was purified by Ni-NTA affinity chromatography under denaturing conditions followed by 60 hours of dialysis. The protein solution turned turbid after dialysis and the pure protein was collected by centrifugation and lyophilized. The lyophilized repeat protein was reconstituted in 150 mM PBS (150 mM K_2HPO_4/KH_2PO_4, and 150 mM NaCl) buffer pH 7.4 heated at 80 °C for 10 minutes to reach a clear solution, which turned turbid when the temperature was decreased. Protein concentrations were determined by diluting the sample until it was clear, measuring tyrosine absorbance at 280 nm and back calculating total concentrations using molar extinction coefficients from ProtParam and dilution factors.

Characterization of condensates. Condensates were imaged using a Zeiss Axio Observer Z1 inverted microscope where 40 µL of the turbid sample was drop-casted on the 10 mm microwell of 35 mm petridish (P35G-1.5-10-C from MatTek). The upper critical saturation temperature was determined by measuring the change in the optical density at 600 nm from 15 °C to 90 °C using a labbot (Probation Labs Sweden AB) UV-visible spectrophotometer. A homogeneous sample was heated at 90 °C which was cooled down stepwise till a final temperature of 15 °C. The saturation concentration (C_{sat}) was measured for all proteins by pelleting the dense phase by centrifugation

follow by measurement of A_{280nm} in the dilute phase using the Labbot instrument (Labbot, Probation Labs Sweden AB).

Dense phase concentration determination. The dense phase concentration of the droplets was determined by centrifuging phase separated samples at 13,000g for 10 mins at a set temperature to get the continuous dense and dilute phase. A known volume of dense phase was taken out using positive displacement pipette and diluted in denaturation buffer (150 mM K_2HPO_4/KH_2PO_4,150 mM NaCl, 8 M urea) to get a homogeneous solution, followed by concentration measurement by UV-Visible spectroscopy at 280 nm.

Electrochemical sensing of oxygen: Oxygen concentrations in the dense and dilute phases were measured using in-house built oxygen microsensor of diameter 10 µm (22). These sensors are also available at UNISENSE (Aarhus, Denmark). The calibrated (2 points in O2 free and air-saturated water) sensor was mounted on micromanipulator (MM33, UNISENSE) controlled by SensorTrace Suite via a motor controller (MOTCON). A macroscopically phase separated sample was prepared by centrifuging 100 µM of $[Q_{5,8}]$-30 solution at 4000 g for 10 mins. The sensor was inserted into the sample and moved across the phase boundary using the micromanipulator resulting in measurements of the oxygen concentration at different depths of the solution starting from several micrometers above the phase boundary.

Phosphorescence lifetime imaging microscopy (PLIM): Samples for PLIM experiments were prepared by adding 500 µM dichlorotris (1,10-phenanthroline) ruthenium (II) hydrate (Sigma Aldrich) to condensate solutions (23). The concentration of the condensate sample used was just above the critical concentration to avoid spinodal decomposition and allow the formation of droplets in nucleation metastable region. Freshly made condensate samples were used to avoid sample variation due to aging of the condensates.

PLIM was performed using a Zeiss observer Z1 inverted microscope equipped with pco.FLIM lasers and frequency domain based luminescence lifetime camera system (24). The frequency modulation was set at 200 kHz based on the known unquenched lifetime of around 1 µs for the ruthenium dye. Starna fluorescent red (UMM/SFR/200X) has similar excitation wavelength as the

ruthenium dye used and was used as a reference with a known lifetime of 5.25 ns. The laser exposure time was adjusted to 1 sec to get good intensity signals. The phosphorescent intensity of the ruthenium dye used as an indicator in the sample should be less than the intensity of the reference dye sample used to avoid background noise in the experiment. Oxygen concentrations were measured using a firestring needle type oxygen sensor with tip diameter of 430 µm (Pyroscience, GmbH), mentioned as reference oxygen sensor in the text, in the dilute phase of the samples. The oxygen sensor was calibrated using two known oxygen concentrations, air saturated water and an oxygen free solution (alkaline ascorbate solution).

We used a chemical oxygen scavenger i.e., sodium sulphite to create different oxygen concentration environment in the samples. We incubated the sample with different concentrations of sodium sulphite and measured the oxygen concentration in the dilute phase of the same sample using the reference oxygen sensor, where 10 mM sodium sulphite resulted in anoxic environment in the dilute phase. Further, we recorded the lifetime values in the dense phase of the same sample using PLIM to determine the partitioning coefficient from the Stern-Volmer plot. Further the oxygen concentration in the dense phase (i.e., inside the condensates) was extrapolated from the partitioning coefficient values obtained. PLIM images were analyzed using imageJ (Fiji software): Background noise was reduced using a Gaussian filter (sigma radius of 70), and the filtered image was subtracted from the original raw intensity image to reduce the background noise. The resulting intensity image obtained was redirected to lifetime channel to measure the lifetime of the dye inside the droplets. We analyzed the droplets by filtering for circularity and diameter and obtained the average lifetime and size for individual droplets. The mean lifetime of the dye in the droplets was plotted versus area of the droplets for both the anoxic and oxic conditions. Finally, we averaged the lifetime values for different sizes of the droplets and plotted the average lifetime of the dye inside the condensates against the known oxygen concentration in the dilute phase.

Partitioning of fluorescent dyes into condensates: We monitor the partitioning of three small molecule fluorescent dyes i.e. sypro orange, fluorescein, and rhodamine B into $[Q_{5,8}]$-20 and $[Q_{5,8}]$-60 condensates using confocal microscopy (Zeiss LSM 90). The concentration of fluorescein and rhodamine B dye used for the experiment was 20 µM and 10X concentration of sypro orange. The images were captured using 60X objective. The fluorescence intensity inside and outside the

condensates is estimated using Fiji software and used to calculate the partition coefficient of fluorophores inside the condensates.

MD Simulations: Topologies and initial conformations for Martini 3 models of [$Q_{5,8}$]-20 IDPs were generated using Polyply, including updated bonded parameters for disordered proteins (25,26). Additionally, non-bonded protein-water interactions were increased by a factor of 1.04 to both improve the global dimensions of disordered proteins, and reduce protein-protein interactions to avoid aggregates (27,28). A factor of 1.04 was used instead of the generally recommended 1.10 as this degree of increase was found to produce homogeneous systems with no protein phase separation. As described elsewhere, the increase in the interaction strength was achieved using a virtual site built directly on top of the protein backbone bead with a specific interaction to water (29). Molecular oxygen was represented by a TC3 bead, based on water-octanol partitioning (26).

To simulate a system representative of a protein in the dilute region of a condensate system, a single protein was placed in a 20 nm cubic box, solvated, neutralized, and salt was added to a concentration of 150 mM NaCl. Oxygen beads were further added to the system at a concentration of 150 mM. For simulations of [$Q_{5,8}$]-20 condensates, a slab configuration was prepared with a condensate of 50 molecules contained within the central 20 nm of a 12 x 12 x 60 nm simulation box. As mentioned before, the system was similarly solvated, neutralized, and ions and oxygen beads were both added to concentrations of 150 mM.

All simulations were performed using Gromacs 2021.7 (30). Systems were energy minimized, followed by equilibration and production simulations. Systems were equilibrated for 100 ns using a timestep of 10 fs and using the Berendsen barostat and thermostat (31). For production runs, a timestep of 20 fs was used for simulations of length 10 μs, using a velocity-rescaling thermostat and Parrinello-Rahman barostat (32,33). For single molecule simulations, the pressure coupling was maintained isotropically at 1 bar, while for slab condensate simulations, semi-isotropic pressure coupling was applied. All simulations were maintained at a temperature of 300 K. Non-bonded simulation parameters otherwise followed the new-rf Martini parameter set, with the exception of the new advised treatment of neighbor lists for the correct calculation of pressure,

such that parameters of rlist =1.35 nm and verlet-buffer-tolerance = -1 were used (34,35). All simulations were performed with three replicates to ensure convergence and consistency in results.

Simulations were analyzed using a combination of Gromacs tools (gmx density) and custom analysis using Python scripts utilizing MD Analysis (36,37). Analysis was performed across the final 2 μs of the simulation time. Radial distribution functions were measured between protein backbone beads and oxygen molecules. To measure contacts between oxygen beads and proteins inside the condensate, a contact was defined as an oxygen being within 6 Å of any protein bead. The length of an individual contact event was defined as the number of consecutive simulation frames where an individual oxygen molecule was in contact with a protein. Similarly, the length of a single condensate visit was defined as the length of time a single oxygen was inside the bulk region of the condensate before leaving again.

Results:

Synthetic IDP as model system for determining oxygen concentration in condensates.

We aimed to study how oxygen partitions into biomolecular condensates (**Fig.1a**), and thus needed a model system that is both representative of natural condensates and experimentally convenient. Many model intrinsically disordered proteins phase separate in the presence of crowding agents like PEG. However, these crowders also affect oxygen solubility (38), which is undesirable in this study. Therefore, we used a synthetic intrinsically disordered protein model system consisting of octa-peptide repeats that form condensates at low saturation concentrations (C_{sat}) without a crowding agent (**Fig.1b**) (21). The repeat protein also allows systematic variation of the number of repeats and the properties of the sequence by changing the amino acid composition. The repeat protein originally contained serine in positions 5 and 8, which we replaced for Gln for compatibility with other experiments. In the following, we refer to these as $[Q_{5,8}]$-X, where X indicates the number of repeats.

Initially, we expressed and purified $[Q_{5,8}]$-30. When reconstituted in PBS these proteins form micrometer-sized spherical assemblies, which fuse upon encounter and grow with incubation time (**Fig. 1c**). These peptide repeats follow upper critical solution temperature (UCST) which means

they form a two-phase system at lower temperature and turn into single homogeneous phase above a critical temperature (**Fig. 1d**). In agreement with previous characterization (21), this suggests that [$Q_{5,8}$]-30 exhibits prototypical UCST liquid-liquid phase separation and is thus a good model for biomolecular condensates formed by many IDPs.

Estimation of oxygen partitioning using a microelectrode: To measure oxygen concentrations inside biomolecular condensates, we initially used an electrochemical Clark-type microsensor with a tip diameter of 10 µm. We created a macroscopically phase separated sample by centrifugation, which resulted in a dilute phase on top of a protein rich dense phase (**Fig. 2a**). The oxygen profile was measured as the sensor was inserted across the phase boundary (**Fig. 2b**). The oxygen concentration was constant in the dilute phase, but gradually dropped with increasing depth (**Fig. 2c**), whereas no change was seen for buffer. The oxygen concentration asymptotically approached a plateau value about 20% lower than the dilute phase. The gradient observed by the microelectrode spans more than two millimeters, which is a much broader transition than expected from partitioning across a phase boundary. The electrochemical measurements indicated that the homogeneous dense phase partially excludes oxygen. However, electrode measurements have limitations as the sensor tip perturbs the macroscopically phase-separated sample and such electrodes are unlikely to work for dispersed condensates due to their size. Therefore, we sought to develop a non-perturbing technique that measures oxygen concentration in co-existing phases.

Measurement of oxygen inside the condensates using phosphorescence lifetime imaging: Phosphorescence lifetime imaging microscopy (PLIM) has been used to quantify the oxygen concentration in for example mammalian cells and organoids (39–43). The phosphorescent dye is quenched by the triplet state of molecular oxygen and the lifetime thus decreases with increasing oxygen concentration (**Fig. 3A**). We speculated that PLIM would also be useful for measuring oxygen partitioning in phase separated systems. As an indicator, we used dichlorotris (1,10-phenanthroline) ruthenium (II) hydrate (**Fig. 3A**), which is a water soluble dye, has excitation and emission in the visible range and has been used for PLIM oxygen imaging (44–46). In the following, we will refer to it as the ruthenium dye. We incubated the ruthenium dye with a phase separated sample of [$Q_{5,8}$]-30, and we imaged the phosphorescence intensity. The condensates appeared as bright spheres against a dark background (**Fig. 3B**) suggesting that the dye

preferentially partitioned into the condensates in agreement with other hydrophobic small molecules (14,18). Some dyes are prone to undesirable self-quenching, which is seen as a concentration dependence of the lifetime. We measured phosphorescence intensity and lifetime for dye concentration from 100 μM to 1 mM. At 100 μM dye, the signal-to-noise ratio was low. At 500 μM the signal was significantly improved without change in the lifetime. Further, the increase to 1 mM resulted in a decrease in lifetime indicating self-quenching (**Fig. S1**). Therefore, we used 500 μM dye in the following experiments.

We imaged [$Q_{5,8}$]-30 condensates at a concentration of 20 μM using PLIM at 40x magnification to record the phosphorescence intensity (**Fig. 3B**) and phosphorescence lifetime (**Fig. 3C**). Condensates can be distinguished as round objects of elevated intensity and changed lifetimes, which allows determination of the lifetime in the dense and dilute phases simultaneously. Cross-sections of droplets reveal a steep gradient in the phosphorescence lifetime between a high value in the dilute phase and a lower value in the dense phase (**Fig. 3C**). In principle, the gradient could represent a boundary layer zone between the phases. However, the spatial resolution of the imaging system is likely not sufficient to resolve the boundary layer, so we only focus on the lifetime in the center of the condensate. The dye experienced a different environment in the dense and dilute phases, which will affect lifetime. Therefore, we measured phosphorescence lifetimes in the absence of oxygen by adding sodium sulphite, a chemical oxygen scavenger (**Fig. 3(D-E))**. In the absence of oxygen, the phosphorescence lifetime increased inside as well as outside the condensates. However, the lifetime of the dye was still less in the dense than in the dilute phase (**Fig. 3E)**. It is necessary to account for this change in basal lifetime when quantifying oxygen concentrations.

To quantify the oxygen concentration, we measured phosphorescence lifetimes in [$Q_{5,8}$]-30 condensates at different sodium sulphite concentrations that only partially scavenge the dissolved oxygen. Simultaneously, we measured the oxygen concentration in the dispersed phase separated sample of [$Q_{5,8}$]-30 using an oxygen optode (pyroscience). This corresponded to the oxygen concentration in the dilute phase, which constituted around 99% of the system. Phosphorescence lifetimes decreased exponentially with increasing oxygen concentration as expected from a collisional quenching mechanism (**Fig. 4A**). We analyzed these data using a Stern-Volmer plot by

plotting τ_0/τ versus different oxygen concentrations measured in the dilute phase of $[Q_{5,8}]$-30 ($[O_2]_{dilute}$) (**Fig. 4B**). The oxygen concentration on the x-axis is thus not the oxygen concentration in the condensate ($[O_2]_{dense}$) where the lifetime is measured, but is related to it by a partitioning coefficient:

$$K_p = \frac{[O_2]_{dense}}{[O_2]_{dilute}}$$

In practice, this becomes part of the slope of the Stern-Volmer plot:

$$\frac{\tau_0}{\tau} = 1 + k_{sv}[O_2]_{dense} = 1 + K_{sv}\, K_P [O_2]_{dilute} \qquad \text{Equation 1}$$

The Stern-Volmer constant, K_{SV}, is the product of oxygen's bimolecular quenching constant and τ_0. As we wish to compare oxygen concentrations in condensates with different τ_0, we thus need to take this into account:

$$\frac{\tau_0}{\tau} = 1 + \tau_0 k_q K_P [O_2]_{dilute} \qquad \text{Equation 2}$$

k_q is determined by how often collisions between molecules result in quenching and is likely to be similar between the two phases. We calculated the oxygen quenching constant for the dilute phase, where the oxygen concentration and τ_0 was known. This allowed us to determine K_P from the slope of the Stern-Volmer plot and subsequently oxygen concentration in the dense phase i.e., $[O_2]_{dense}$. K_P obtained from the slope was approximately 0.38 ± 0.049 and the oxygen concentration in the dilute phase was 265 μM ± 4 μM. Therefore, the $[O_2]_{dense}$ was 103 μM ± 4 μM (**Fig. 4C**). In agreement with microelectrode measurements, this indicated that protein condensates partially exclude oxygen and create low oxygen zones inside them. PLIM suggests a larger depletion than micro-electrodes, however as microelectrodes perturb that phase boundary it likely underestimates the difference between the two phases.

Next, we checked the effect of the size of the droplets on the phosphorescence lifetime due to the heterogeneous nature of the droplets. Phosphorescence lifetime decreases slightly for bigger droplets (**Fig. S2**), but condensates at atmospheric oxygen and anoxic conditions were affected

similarly, so the difference effect mostly cancels out for partitioning coefficients. However, in our further comparisons, we restricted our analysis in the following to droplet sizes that are present in all variants to avoid confounders.

Determinants of K_p

Oxygen is non-polar with a octanol-water partition coefficient of 4.4 (47), which suggested that it is more prone to partition into hydrophobic condensates in line with other small molecules (14,18). Therefore, we wanted to modulate the hydrophobicity without disrupting phase separation. Therefore, we started from a longer repeat protein [$Q_{5,8}$]-60, which forms condensates at very low protein concentration, and substitute glutamine at the 5th position to valine. To get a range of hydrophobicity, we substituted every fourth repeat [(3Q_5:V_5),Q_8]-60, every other repeat [(Q_5:V_5),Q_8]-60 or every repeat [V_5,Q_8]-60. Proteins were purified and characterized by microscopy and UV-visible spectroscopy (**Fig. S3**). All variants produced round condensates, however [V_5Q_8]-60 mostly formed irreversible aggregates and the droplets formed were below a diameter of 2 μm. The irreversible aggregates could be removed by centrifugation at high temperature, however the aggregation propensity indicated that we cannot further increase the hydrophobicity of the peptide repeats. The critical concentration gradually decreased with increasing hydrophobicity **(Fig. S3B).**

Next, we measured the oxygen concentration in the dilute homogeneous solution of [$Q_{5,8}$]-60, [(3Q_5:V_5),Q_8]-60, [(Q_5:V_5),Q_8]-60 and [V_5,Q_8]-60 using a firestring oxygen optode as a control for PLIM experiment. We observed that the oxygen concentration in the dilute phase of all hydrophobic variants is similar around 265 μM ± 10 μM. We focused on droplets with diameters from 1 to 4 μm, which was ubiquitous in all the variants. We measured the lifetime of [$Q_{5,8}$]-60, [(3Q_5:V_5),Q_8]-60, [(Q_5:V_5),Q_8]-60 and [V_5,Q_8]-60 condensates at atmospheric oxygen condition and anoxic conditions to determine the oxygen concentrations in the dense phase. The difference in lifetime from oxic-to-anoxic condition decreased with an increasing hydrophobicity for similar size of the droplets with exception of [V_5:Q_8]-60 **(Fig. 5A-D)**. Next, we averaged the lifetime for all droplets in the similar size distribution range and plotted the ratio of lifetime in anoxic to oxic condition (τ_0/τ) i.e., against dilute phase oxygen concentration to calculate partitioning

coefficients. Unexpectedly, oxygen showed a non-monotonous dependence on condensate hydrophobicity. Oxygen partitioning into the condensates decreased upon substitution of every fourth glutamine but increased upon further substitutions (**Fig. 5E**). Substitutions of residues in the octa-repeat may also affect the condensate interior in other ways than via hydrophobicity. To probe the condensate structure, we measured the protein concentration inside the droplets. The dense phase concentration of [(3Q_5:V_5),Q_8]-60 variant was similar to [$Q_{5,8}$]-60 variant but decreases for [(Q_5:V_5),Q_8]-60 variant. We could not determine the dense phase concentration for [V_5,Q_8]-60 (**Fig. 5G**). The decrease in the oxygen concentration for [3Q_5:V_5),Q_8]-60 with similar dense phase concentration could be the compaction of the condensates and decrease in solvent availability. However, there is no clear correlation between the dense phase concentration and oxygen partitioning observed for other hydrophobic variants due to the change in both the hydrophobicity and dense phase concentrations.

To explore the determinants of oxygen partitioning further, we sought a way to change the phase diagram without changing the chemical environment in the condensates. Uniquely, repeat proteins offer this possibility as the phase diagram is highly sensitive to the number of identical repeats. We thus expressed and purified [$Q_{5,8}$]-20, [$Q_{5,8}$]-30, [$Q_{5,8}$]-40 and [$Q_{5,8}$]-60 and characterized them as above (**Fig. S4**). All the variants formed condensates with condensate size and critical concentration decreasing with chain length. The oxygen concentration as measured by the oxygen optode in the dilute phase of all variants is similar around 265 μM ± 10 μM. We measured the lifetime of the similar sized [$Q_{5,8}$]-20, [$Q_{5,8}$]-30, [$Q_{5,8}$]-40 and [$Q_{5,8}$]-60 condensates at atmospheric oxygen condition and anoxic conditions to determine the oxygen concentrations in the dense phase (**Fig. 6A).** The difference in the lifetime from oxic-to-anoxic condition increased with an increasing number of repeats for similar size of the droplets **(Fig. 6A)**. The average phosphorescence lifetime values for dyes inside the droplets was analysed to calculate K_p and the oxygen concentration inside the condensates **(Fig. 6BC**). The K_p increased monotonously towards one with increased chain length suggesting less exclusion of oxygen for the longest chains. **(Fig. 6C**). The effect was larger and more consistent than for variants with varied hydrophobicity. As these condensates are composed of identical peptide repeats, solvation-like interactions are unlikely to account for the difference.

Instead, the internal structure of the condensates could act as a potential determinant of partitioning. Condensates formed by different chain length are likely to have different nanoscale structures although they appear similar under a microscope. We turned to dense phase protein concentration as an overall reporter of condensate organization. Chain length generally reduces the critical concentration of repeating polymers, but much less is known about how it affects the dense phase concentration. We measured the dense phase concentration for $[Q_{5,8}]$-X and found that it decreased uniformly with chain length (**Fig. 6D**). $[Q_{5,8}]$-20 has protein concentration of ~170 mg/mL, which is similar to values previously reported for other condensates (48–51). For $[Q_{5,8}]$-60, the dense phase protein concentration is much lower (~70 mg/mL) suggesting that the long repeat proteins form a much looser condensate.

A less tight-knit condensate provides more accessible solvent to small molecule clients such as oxygen. Accordingly, we observed an anti-correlation between oxygen and protein concentrations in the dense phase (**Fig. 6E**), which suggests that partitioning of oxygen is dominated by the excluded volume from the protein chain. Such interactions are likely to be general and may contribute to the partitioning of other small molecules. To test this hypothesis, we measured partitioning of three relatively hydrophobic fluorophores in $[Q_{5,8}]$-20 and $[Q_{5,8}]$-60 using fluorescence microscopy. All three fluorophores partition favorably into both condensates, although to different extents with K_P varying from ~2 to 70. Interestingly, the partitioning coefficient was correlated with preference for $[Q_{5,8}]$-20 over $[Q_{5,8}]$-60 (**Fig. S5**). Partitioning of these dye molecules is driven by solvent-like interactions between the scaffold and the client, which also changes with the protein concentration in the dense phase. This suggests that the accessible solvent volume only dominates small molecule partitioning in the absence of strong interactions with the scaffold.

Molecular dynamics simulations of oxygen partitioning.

To investigate how oxygen interacts with the condensates in atomistic detail, we thus undertook molecular dynamics (MD) simulation of oxygen partitioning. MD methods range from all-atom models that can represent any type of chemistry to highly coarse-grained models where each residue is represented by a single bead. Although it is possible to simulate at an all-atom resolution,

these force fields are generally too computationally expensive to handle the system size needed to achieve phase separation (52). At a much coarser resolution, one-bead-per-residue methods are efficient at capturing the phase behavior of IDPs , they are inherently unable to describe the interactions of small molecule clients such as oxygen (53–56). Between these options is the Martini force field, which uses a transferable building block approach representing 2-4 heavy atoms by a single bead, combining beads to build entire molecules, parameterized based on underlying chemical properties (26,57,58). Martini has already shown promise in simulating several condensate systems (28,59–61). Building on this, we showed that Martini resolution simulations can reproduce the phase separation of [$Q_{5,8}$]-20 IDPs as expected (**Fig. S6**).

Qualitatively, the simulations agree with the experimental results in predicting an 50% lower oxygen concentration inside the condensate relative to the outside (**Fig. 7A**). Moreover, the visits of oxygen to the bulk region of the condensate are typically very short lived. As **Fig. 7B** shows, single visits to the bulk of the condensate are predominantly less than 10 ns in total before the molecule leaves to the dilute region of the system again, with longer occupations becoming exponentially rare. This suggests that oxygen mostly remains highly dynamic inside the condensate.

To understand the potential interaction between oxygen and the condensate forming proteins, we looked at the distribution of oxygen around each of the residues in the octapeptide repeat unit of the [$Q_{5,8}$]-20 protein using radial distribution functions (**Fig. 7C, Fig. S7**). While there is relatively little change in the residue-specific radial distribution functions, there is a slight indication that oxygen is more prevalent around tyrosine compared to other residues in the octapeptide repeat. The same sequence of preference around the repeat unit residues is also observed for a single protein in the dilute phase of the condensate, further indicating that the overall interaction of oxygen with disordered proteins is weak and the condensate does not change the preference for interactions compared to the monomeric state (**Fig. S8)**. This further confirms that condensates remain highly dynamic through local rearrangements of interactions (52).

Discussion:

In the present work, we have observed that the condensates partially exclude oxygen and create a low oxygen zone inside. While recent studies of small molecule partitioning have studied many small molecules in a limited set of very different condensates, we took a different strategy and studied a single biochemically important molecule in several condensates with systematic variations. We thus changed the physical and chemical properties of the synthetic IDPs that form the condensates, which showed that oxygen partitioning is dominated by the solvent accessible volume rather than interactions with the scaffold. This suggests that partitioning of small molecules is not just determined by the internal chemical environment of the condensates, but also their physical architecture. This highlights that biomolecular condensates are not simple liquids even though they may macroscopically appear similar. Partitioning into a simple liquid such as octanol can be described well by focusing on hydrophobicity, however a biomolecular condensate has complex internal organization derived from their macromolecular constituents that can affect biochemical reactions.

This work required establishment of methods to measure oxygen concentrations in coexisting phases. The PLIM technique used can readily resolve co-existing phases and is mostly concentration independent as it relies on lifetime measurements. Unlike many fluorescent reporters, the PLIM sensor does not bind oxygen and should thus not affect the partitioning. The PLIM analysis method proposed here relies on an assumption that the quenching constant k_q is similar for both the dilute and the dense phase. This assumption is hard to test experimentally but relies on the assumption of similar diffusion of small molecules. Condensates retard the diffusion of small molecules a lot, however small molecules have comparable diffusion constants to dilute buffers (62), suggesting that such effects would be minimal. Second, we rely on a chemical scavenger sodium sulfite to create anoxic conditions. We also tried to image condensates in a chamber with atmospheric control, however, we found that the time required for oxygen depletion of the liquid phase led to unacceptable evaporation and coarsening of the condensate. Despite these limitations, we think the PLIM technique is a useful tool for measuring oxygen inside coexisting phases. Additionally, we found similar oxygen depletion using electrochemical sensing and MD simulations studies suggesting that the overall conclusions are correct even if small systematic errors cannot be excluded.

The measurement methods used in this study rely on oxygen participating in either an electrochemical reaction or collisional quenching. Both of these reactions are likely not to depend on the concentration per se, but rather the chemical activity. Recent theoretical work has suggested that the chemical activity of small molecule clients in condensate may differ significantly from their concentrations as the interactions that drive favorable partitioning are also likely to sequester the client molecule from chemical reactions (63). For example, in a study of oxygen sensitive enzymatic reactions in peptide hydrogels, it was observed that oxygen does not affect the reaction due to the binding of the oxygen to hydrophobic pockets in the gel (64). While similar effects could have been expected in condensates, our MD simulations suggested that we do not see particularly strong interactions between scaffold and oxygen molecules. This suggested that the activities we measure are a good approximation of the concentration.

Oxygen partitions favorably into octanol compared to water, suggesting more favorable solvation by hydrophobic solvents (47). Oxygen is symmetrical and thus relatively featureless in terms of interactions, and therefore hydrophobicity is the driving force for partitioning into octanol. Hydrophobicity has also been suggested as a general determinant of small molecule partitioning into condensates, however specific interactions also affect it (14). Our PLIM studies on repeat protein condensate model has allowed us to identify excluded volume, rather than hydrophobicity, as a central determinant for molecular oxygen partitioning. However, this effect should be general for practically all other systems but are often masked by additional effects.

The study's findings shed light on how membrane-less organelles influence oxidative stress in physiology, offering insights into cellular processes like aging and disease. Additionally, this understanding could also impact biotechnological applications by elucidating the effect of these organelles on oxygen-dependent reactions.

Acknowledgements:

This work was supported by grants from the Villum Foundation (40662) to M.K., and a Novo Nordisk Foundation Interdisciplinary synergy grant (NNF20OC0063808) to M.K. and S.J.M, Grundfos Foundation and Carlsberg Foundation to K.K. We thank SURF (www.surf.nl) for the support in

using the National Supercomputer Snellius. Authors would like to thank Lars Borregaard Pedersen and Mette Hoffmann Asmussen for excellent technical support.

References:

1. Giomi F, Barausse A, Steckbauer A, Daffonchio D, Duarte CM, Fusi M. Oxygen dynamics in marine productive ecosystems at ecologically relevant scales. Nat Geosci. 2023 Jul;16(7):560–6.

2. Klanten Y, Couture R -M., Christoffersen KS, Vincent WF, Antoniades D. Oxygen Depletion in Arctic Lakes: Circumpolar Trends, Biogeochemical Processes, and Implications of Climate Change. Global Biogeochemical Cycles. 2023 May;37(5):e2022GB007616.

3. Jørgensen BB, Wenzhöfer F, Egger M, Glud RN. Sediment oxygen consumption: Role in the global marine carbon cycle. Earth-Science Reviews. 2022 May;228:103987.

4. Dunn JO, Mythen M, Grocott M. Physiology of oxygen transport. BJA Education. 2016 Oct;16(10):341–8.

5. Zhdanov AV, Golubeva AV, Okkelman IA, Cryan JF, Papkovsky DB. Imaging of oxygen gradients in giant umbrella cells: an ex vivo PLIM study. American Journal of Physiology-Cell Physiology. 2015 Oct 1;309(7):C501–9.

6. Thar R, Kühl M. Bacteria are not too small for spatial sensing of chemical gradients: An experimental evidence. Proc Natl Acad Sci USA. 2003 May 13;100(10):5748–53.

7. Banani SF, Lee HO, Hyman AA, Rosen MK. Biomolecular condensates: organizers of cellular biochemistry. Nat Rev Mol Cell Biol. 2017 May;18(5):285–98.

8. Shin Y, Brangwynne CP. Liquid phase condensation in cell physiology and disease. Science. 2017 Sep 22;357(6357):eaaf4382.

9. Laflamme G, Mekhail K. Biomolecular condensates as arbiters of biochemical reactions inside the nucleus. Commun Biol. 2020 Dec 15;3(1):773.

10. Alberti S, Hyman AA. Biomolecular condensates at the nexus of cellular stress, protein aggregation disease and ageing. Nat Rev Mol Cell Biol. 2021 Mar;22(3):196–213.

11. Brangwynne CP, Eckmann CR, Courson DS, Rybarska A, Hoege C, Gharakhani J, et al. Germline P Granules Are Liquid Droplets That Localize by Controlled Dissolution/Condensation. Science. 2009 Jun 26;324(5935):1729–32.

12. Nott TJ, Petsalaki E, Farber P, Jervis D, Fussner E, Plochowietz A, et al. Phase Transition of a Disordered Nuage Protein Generates Environmentally Responsive Membraneless Organelles. Molecular Cell. 2015 Mar;57(5):936–47.

13. Küffner AM, Prodan M, Zuccarini R, Capasso Palmiero U, Faltova L, Arosio P. Acceleration of an Enzymatic Reaction in Liquid Phase Separated Compartments Based on Intrinsically Disordered Protein Domains. ChemSystemsChem. 2020 Jul;2(4):e2000001.

14. Kilgore HR, Mikhael PG, Overholt KJ, Boija A, Hannett NM, Van Dongen C, et al. Distinct chemical environments in biomolecular condensates. Nat Chem Biol [Internet]. 2023 Sep 28 [cited 2023 Dec 4]; Available from: https://www.nature.com/articles/s41589-023-01432-0

15. Kilgore HR, Young RA. Learning the chemical grammar of biomolecular condensates. Nat Chem Biol. 2022 Dec;18(12):1298–306.

16. Klein IA, Boija A, Afeyan LK, Hawken SW, Fan M, Dall'Agnese A, et al. Partitioning of cancer therapeutics in nuclear condensates. Science. 2020 Jun 19;368(6497):1386–92.

17. Dumelie JG, Chen Q, Miller D, Attarwala N, Gross SS, Jaffrey SR. Biomolecular condensates create phospholipid-enriched microenvironments. Nat Chem Biol. 2024 Mar;20(3):302–13.

18. Thody SA, Clements HD, Baniasadi H, Lyon AS, Sigman MS, Rosen MK. Small Molecule Properties Define Partitioning into Biomolecular Condensates [Internet]. Biochemistry; 2022 Dec [cited 2023 Dec 4]. Available from: http://biorxiv.org/lookup/doi/10.1101/2022.12.19.521099

19. Quaranta M, Borisov SM, Klimant I. Indicators for optical oxygen sensors. Bioanal Rev. 2012 Dec;4(2–4):115–57.

20. Wang X dong, Wolfbeis OS. Optical methods for sensing and imaging oxygen: materials, spectroscopies and applications. Chem Soc Rev. 2014;43(10):3666–761.

21. Dzuricky M, Rogers BA, Shahid A, Cremer PS, Chilkoti A. De novo engineering of intracellular condensates using artificial disordered proteins. Nat Chem. 2020 Sep;12(9):814–25.

22. Revsbech NP. An oxygen microsensor with a guard cathode. Limnology & Oceanography. 1989 Mar;34(2):474–8.

23. Demas JN, Diemente D, Harris EW. Oxygen quenching of charge-transfer excited states of ruthenium(II) complexes. Evidence for singlet oxygen production. J Am Chem Soc. 1973 Oct;95(20):6864–5.

24. Moßhammer M, Scholz VV, Holst G, Kühl M, Koren K. Luminescence Lifetime Imaging of O_2 with a Frequency-Domain-Based Camera System. JoVE. 2019 Dec 16;(154):60191.

25. Grünewald F, Alessandri R, Kroon PC, Monticelli L, Souza PCT, Marrink SJ. Polyply; a python suite for facilitating simulations of macromolecules and nanomaterials. Nat Commun. 2022 Jan 10;13(1):68.

26. Souza PCT, Alessandri R, Barnoud J, Thallmair S, Faustino I, Grünewald F, et al. Martini 3: a general purpose force field for coarse-grained molecular dynamics. Nat Methods. 2021 Apr;18(4):382–8.

27. Thomasen FE, Pesce F, Roesgaard MA, Tesei G, Lindorff-Larsen K. Improving Martini 3 for Disordered and Multidomain Proteins. J Chem Theory Comput. 2022 Apr 12;18(4):2033–41.

28. Ingólfsson HI, Rizuan A, Liu X, Mohanty P, Souza PCT, Marrink SJ, et al. Multiscale simulations reveal TDP-43 molecular-level interactions driving condensation. Biophysical Journal. 2023 Nov;122(22):4370–81.

29. Souza PCT, Borges-Araújo L, Brasnett C, Moreira RA, Grünewald F, Park P, et al. GōMartini 3: From large conformational changes in proteins to environmental bias corrections [Internet]. 2024 [cited 2024 Apr 29]. Available from: http://biorxiv.org/lookup/doi/10.1101/2024.04.15.589479

30. Abraham MJ, Murtola T, Schulz R, Páll S, Smith JC, Hess B, et al. GROMACS: High performance molecular simulations through multi-level parallelism from laptops to supercomputers. SoftwareX. 2015 Sep;1–2:19–25.

31. Berendsen HJC, Postma JPM, Van Gunsteren WF, DiNola A, Haak JR. Molecular dynamics with coupling to an external bath. The Journal of Chemical Physics. 1984 Oct 15;81(8):3684–90.

32. Parrinello M, Rahman A. Polymorphic transitions in single crystals: A new molecular dynamics method. Journal of Applied Physics. 1981 Dec 1;52(12):7182–90.

33. Bussi G, Donadio D, Parrinello M. Canonical sampling through velocity rescaling. The Journal of Chemical Physics. 2007 Jan 7;126(1):014101.

34. De Jong DH, Baoukina S, Ingólfsson HI, Marrink SJ. Martini straight: Boosting performance using a shorter cutoff and GPUs. Computer Physics Communications. 2016 Feb;199:1–7.

35. Kim H, Fábián B, Hummer G. Neighbor List Artifacts in Molecular Dynamics Simulations. J Chem Theory Comput. 2023 Dec 12;19(23):8919–29.

36. Michaud-Agrawal N, Denning EJ, Woolf TB, Beckstein O. MDAnalysis: A toolkit for the analysis of molecular dynamics simulations. J Comput Chem. 2011 Jul 30;32(10):2319–27.

37. Gowers R, Linke M, Barnoud J, Reddy T, Melo M, Seyler S, et al. MDAnalysis: A Python Package for the Rapid Analysis of Molecular Dynamics Simulations. In Austin, Texas; 2016 [cited 2024 Mar 24]. p. 98–105. Available from: https://conference.scipy.org/proceedings/scipy2016/oliver_beckstein.html

38. Christmas KM, Bassingthwaighte JB. Equations for O_2 and CO_2 solubilities in saline and plasma: combining temperature and density dependences. Journal of Applied Physiology. 2017 May 1;122(5):1313–20.

39. Dmitriev RI, Kondrashina AV, Koren K, Klimant I, Zhdanov AV, Pakan JMP, et al. Small molecule phosphorescent probes for O_2 imaging in 3D tissue models. Biomater Sci. 2014;2(6):853–66.

40. Dmitriev RI, editor. Multi-Parametric Live Cell Microscopy of 3D Tissue Models [Internet]. Cham: Springer International Publishing; 2017 [cited 2024 Feb 2]. (Advances in Experimental Medicine and Biology; vol. 1035). Available from: http://link.springer.com/10.1007/978-3-319-67358-5

41. Dmitriev RI, Zhdanov AV, Jasionek G, Papkovsky DB. Assessment of Cellular Oxygen Gradients with a Panel of Phosphorescent Oxygen-Sensitive Probes. Anal Chem. 2012 Mar 20;84(6):2930–8.

42. Koren K, Dmitriev RI, Borisov SM, Papkovsky DB, Klimant I. Complexes of Ir^{III} - Octaethylporphyrin with Peptides as Probes for Sensing Cellular O_2. ChemBioChem. 2012 May 29;13(8):1184–90.

43. Papkovsky DB, Dmitriev RI. Biological detection by optical oxygen sensing. Chem Soc Rev. 2013;42(22):8700.

44. Hara D, Umehara Y, Son A, Asahi W, Misu S, Kurihara R, et al. Tracking the Oxygen Status in the Cell Nucleus with a Hoechst-Tagged Phosphorescent Ruthenium Complex. ChemBioChem. 2018 May 4;19(9):956–62.

45. Paxian M, Keller SA, Cross B, Huynh TT, Clemens MG. High-resolution visualization of oxygen distribution in the liver in vivo. American Journal of Physiology-Gastrointestinal and Liver Physiology. 2004 Jan;286(1):G37–44.

46. Yaegashi K, Itoh T, Kosaka T, Fukushima H, Morimoto T. Diffusivity of oxygen in microvascular beds as determined from PO2 distribution maps. American Journal of Physiology-Heart and Circulatory Physiology. 1996 Apr 1;270(4):H1390–7.

47. International Chemical Safety cards [Internet]. [cited 2024 Apr 23]. International Chemical safety cards database. Available from: https://www.ilo.org/dyn/icsc/showcard.home

48. Vazquez DS, Toledo PL, Gianotti AR, Ermácora MR. Protein conformation and biomolecular condensates. Current Research in Structural Biology. 2022;4:285–307.

49. Burke KA, Janke AM, Rhine CL, Fawzi NL. Residue-by-Residue View of In Vitro FUS Granules that Bind the C-Terminal Domain of RNA Polymerase II. Molecular Cell. 2015 Oct;60(2):231–41.

50. Kim TH, Payliss BJ, Nosella ML, Lee ITW, Toyama Y, Forman-Kay JD, et al. Interaction hot spots for phase separation revealed by NMR studies of a CAPRIN1 condensed phase. Proc Natl Acad Sci USA. 2021 Jun 8;118(23):e2104897118.

51. Wong LE, Kim TH, Muhandiram DR, Forman-Kay JD, Kay LE. NMR Experiments for Studies of Dilute and Condensed Protein Phases: Application to the Phase-Separating Protein CAPRIN1. J Am Chem Soc. 2020 Feb 5;142(5):2471–89.

52. Galvanetto N, Ivanović MT, Chowdhury A, Sottini A, Nüesch MF, Nettels D, et al. Extreme dynamics in a biomolecular condensate. Nature. 2023 Jul 27;619(7971):876–83.

53. Joseph JA, Reinhardt A, Aguirre A, Chew PY, Russell KO, Espinosa JR, et al. Physics-driven coarse-grained model for biomolecular phase separation with near-quantitative accuracy. Nat Comput Sci. 2021 Nov 22;1(11):732–43.

54. Tesei G, Lindorff-Larsen K. Improved predictions of phase behaviour of intrinsically disordered proteins by tuning the interaction range. Open Res Europe. 2023 Jan 17;2:94.

55. Borges-Araújo L, Patmanidis I, Singh AP, Santos LHS, Sieradzan AK, Vanni S, et al. Pragmatic Coarse-Graining of Proteins: Models and Applications. J Chem Theory Comput. 2023 Oct 24;19(20):7112–35.

56. Dignon GL, Best RB, Mittal J. Biomolecular Phase Separation: From Molecular Driving Forces to Macroscopic Properties. Annu Rev Phys Chem. 2020 Apr 20;71(1):53–75.

57. Marrink SJ, Risselada HJ, Yefimov S, Tieleman DP, De Vries AH. The MARTINI Force Field: Coarse Grained Model for Biomolecular Simulations. J Phys Chem B. 2007 Jul 1;111(27):7812–24.

58. Marrink SJ, Monticelli L, Melo MN, Alessandri R, Tieleman DP, Souza PCT. Two decades of Martini: Better beads, broader scope. WIREs Comput Mol Sci. 2023 Jan;13(1):e1620.

59. Benayad Z, Von Bülow S, Stelzl LS, Hummer G. Simulation of FUS Protein Condensates with an Adapted Coarse-Grained Model. J Chem Theory Comput. 2021 Jan 12;17(1):525–37.

60. Tsanai M, Frederix PWJM, Schroer CFE, Souza PCT, Marrink SJ. Coacervate formation studied by explicit solvent coarse-grain molecular dynamics with the Martini model. Chem Sci. 2021;12(24):8521–30.

61. Zerze GH. Optimizing the Martini 3 Force Field Reveals the Effects of the Intricate Balance between Protein–Water Interaction Strength and Salt Concentration on Biomolecular Condensate Formation. J Chem Theory Comput. 2024 Feb 27;20(4):1646–55.

62. Wei MT, Elbaum-Garfinkle S, Holehouse AS, Chen CCH, Feric M, Arnold CB, et al. Phase behaviour of disordered proteins underlying low density and high permeability of liquid organelles. Nature Chem. 2017 Nov;9(11):1118–25.

63. Bauermann J, Laha S, McCall PM, Jülicher F, Weber CA. Chemical Kinetics and Mass Action in Coexisting Phases. J Am Chem Soc. 2022 Oct 26;144(42):19294–304.

64. Ben-Zvi O, Grinberg I, Orr AA, Noy D, Tamamis P, Yacoby I, et al. Protection of Oxygen-Sensitive Enzymes by Peptide Hydrogel. ACS Nano. 2021 Apr 27;15(4):6530–9.

Figures

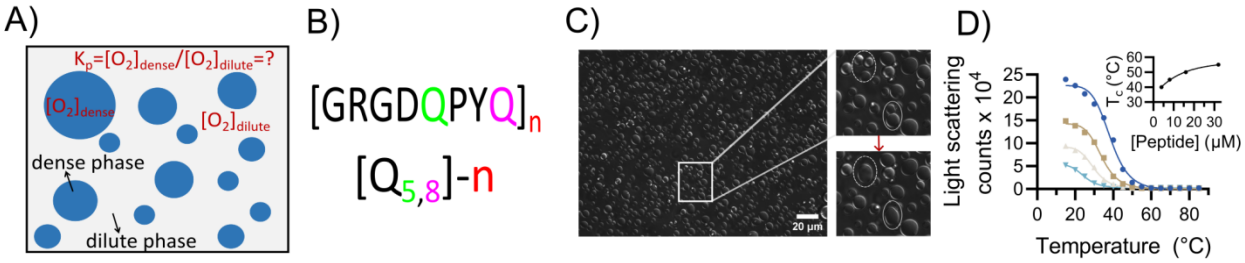

Figure 1: Characterization of octa-repeat protein condensates. (A) Oxygen concentrations in the dense and dilute phases are related by the partitioning coefficient (K_p). (B) Artificial IDPs based on octa-peptide repeats form condensates and serve as a model system for oxygen partitioning. (C) DIC microscopy images of $[Q_{5,8}]$-30 droplets. Enlarged view shows subsequent images in a time series showing fusion of droplets. (D) Temperature dependent light scattering of $[Q_{5,8}]$-30 protein concentration of 4µM (light blue), 8 µM(beige), 16 µM (brown) and 32 µM (dark blue). (D) Inset shows protein concentration-dependent change in the critical temperature (T_c).

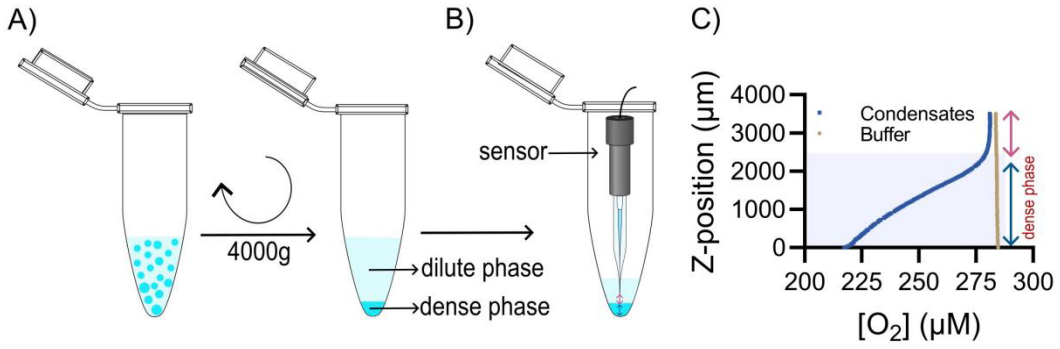

Figure 2: Determination of oxygen concentration in condensates using electrochemical sensing. (A) A macroscopically condensate was prepared by centrifugation 4000 g of a phase separated sample of $[Q_{5,8}]$-30. (B) Oxygen concentrations were measured across the phase boundary by inserting an electrochemical microelectrode into the continuous dense phase of $[Q_{5,8}]$-30. (C) Change in the oxygen concentration (µM) with change in the sensor position from dilute phase to the dense phase (µm), where shaded blue area corresponds approximately to the pelleted $[Q_{5,8}]$-30 condensate.

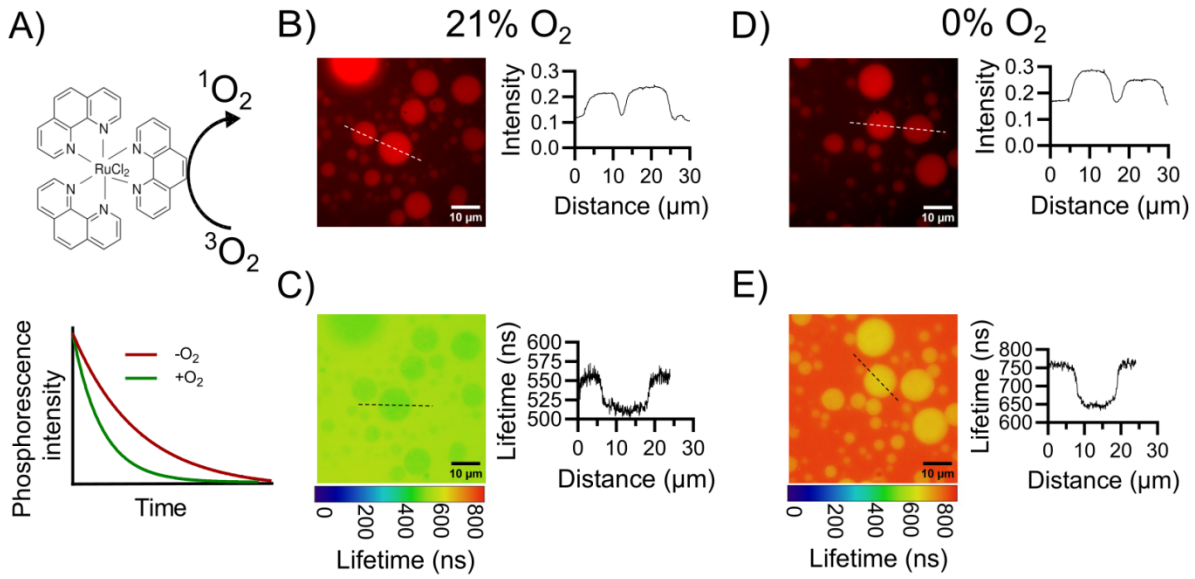

Figure 3: Determination of oxygen concentrations in condensates using PLIM. (A) Phosphorescence from ruthenium-dyes are sensitive to the oxygen concentration and the excited stated is quenched by contact with triplet state oxygen. Phosphorescence lifetimes thus decrease in the presence of oxygen, which allows oxygen concentrations to be imaged using PLIM. The chemical structure represents the dye used throughout this study named Tris dichlorotris (1,10-phenanthroline) ruthenium (II) hydrate where (B, D) represented Phosphorescence intensity and (C, E) corresponded for lifetime images of a phase separated sample of [$Q_{5,8}$]-30. (B, C) were recorded on samples in equilibrium atmospheric oxygen concentrations, and (D, E) under anoxic conditions. Intensity and lifetime line profiles were extracted at the indicated dashed lines.

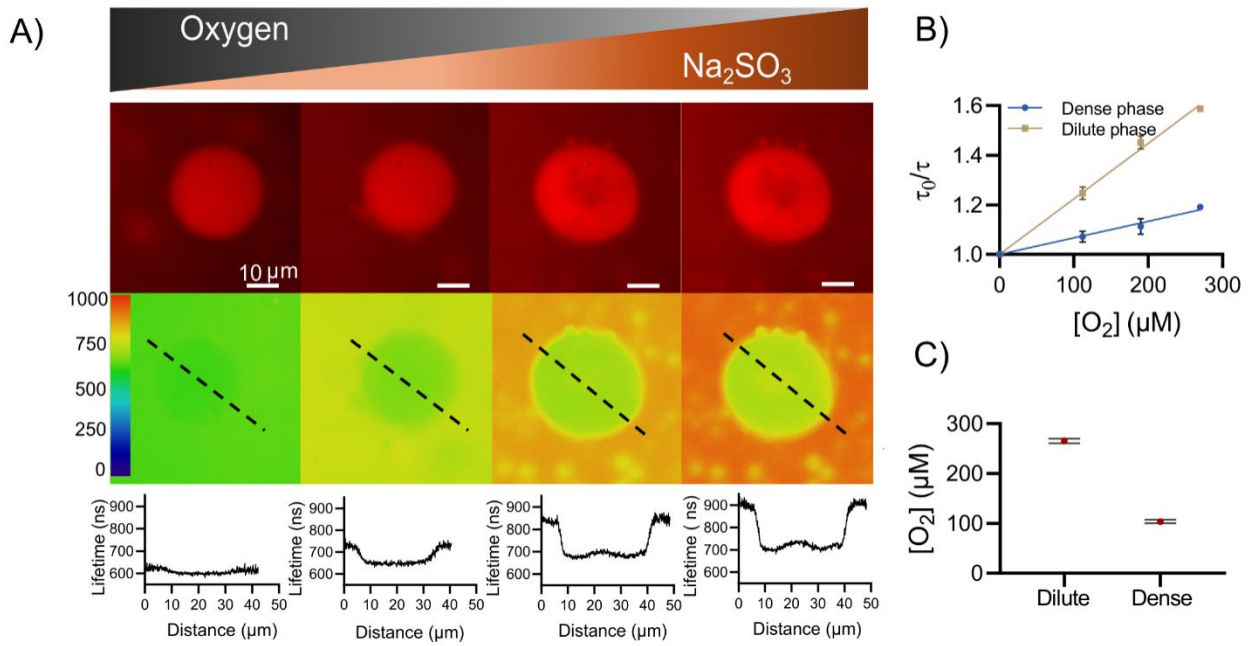

Figure 4: Oxygen dependent phosphorescence lifetime in the droplets. (A) Phosphorescence lifetime imaging of the [$Q_{5,8}$]-30 condensate sample at different oxygen concentrations created by created by titrating with sodium sulfite (Na_2SO_3), where phosphorescence intensity is shown in top panel, phosphorescence lifetime in middle panel and line profile of the lifetime across droplet in bottom panel. (B) Stern Volmer plot where τ_0/τ plotted with change in oxygen concentration for dense phase droplet (blue) and dilute phase (brown) of the [$Q_{5,8}$]-30 condensates. (C) Oxygen concentrations in the dense and dilute phases as determined from the Stern-Volmer plot. Error bars represent standard deviation (S.D.) from triplicate readings.

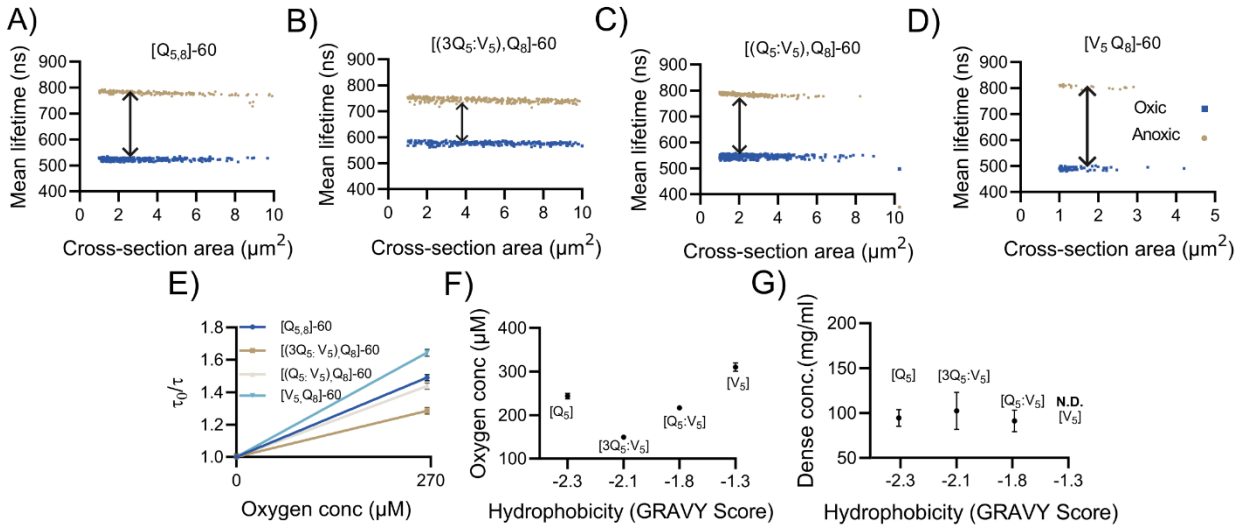

Figure 5: Effect of hydrophobicity on the partitioning of oxygen in the droplets. (A-D) Mean phosphorescence lifetime versus condensate size for condensates with different hydrophobicity. (E) Stern-Volmer plot for all the hydrophobic variants to estimate the effect of hydrophobicity on oxygen quenching. (F) Concentration of oxygen in the droplets was plotted with change in hydrophobicity (GRAVY score) number. (G) Dense phase concentration of different variants is plotted with change in hydrophobicity (GRAVY score), where the dense phase concentration for [V_5] variant cannot be determined. Error bars represent standard deviation (S.D.) from triplicate readings.

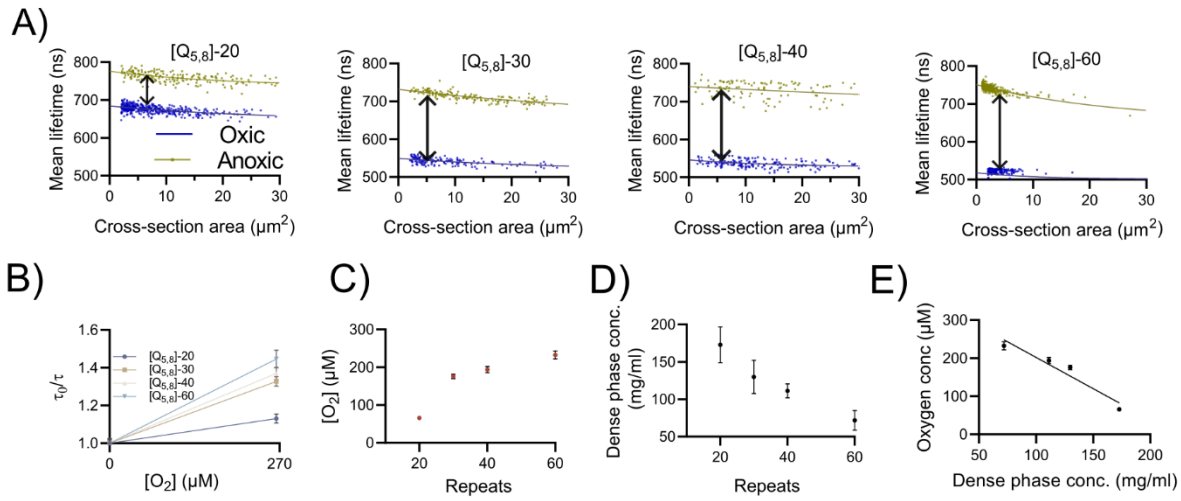

Figure 6: Effect of chain length on the partitioning of oxygen. Correlation between mean phosphorescence lifetime and droplet size for condensates formed by (A) $[Q_{5,8}]$-20, $[Q_{5,8}]$-30, $[Q_{5,8}]$-40, and $[Q_{5,8}]$-60. The difference between the lifetime under anoxic and oxic conditions increased with repeats as shown with double-sided black arrows. (B) Stern Volmer plot for all the repeats to estimate the effect of repeats on phosphorescence lifetime and partitioning coefficient determined from the slope of the curves. (C) Oxygen concentration in the droplets with change in the number of repeats. (D) Dense phase concentration of different variants is plotted with increase in number of repeats and (E) Oxygen concentration is plotted with change in dense phase concentration of droplets. Error bars represent standard deviation (S.D.) from triplicate readings. **Note**: The dense phase determination for the repeats (figure 6) and the hydrophobic variants (figure 5) has been done separately.

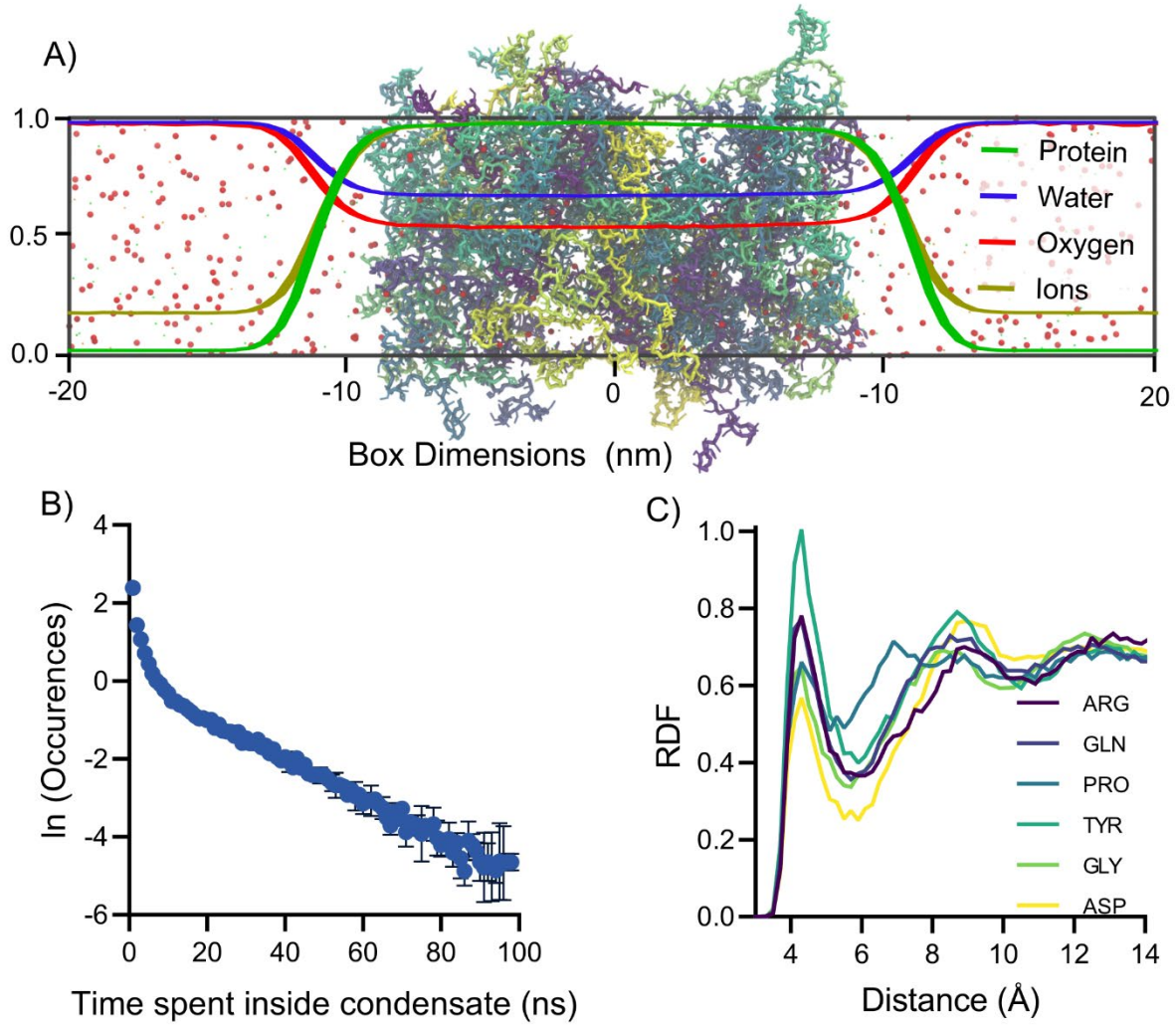

Figure 7. Coarse-grained simulations of oxygen molecules in condensates. (A) Normalized density profiles of the simulated system components across a slab condensate system. (B) Lengths of visits of oxygen molecules to the bulk region of the condensate. (C) Radial distribution functions plotted for the distribution of oxygen around different residues of the octapeptide repeat unit.